



1 **Characterizing the performance of a POPS**  
2 **miniaturized optical particle counter when**  
3 **operated on a quadcopter drone**

4 **Zixia Liu<sup>1</sup>, Martin Osborne<sup>1,2</sup>, Jim Haywood<sup>1,2</sup>, Karen Anderson<sup>3</sup>,**  
5 **Jamie D. Shutler<sup>3</sup>, Andy Wilson<sup>2</sup>, Justin Langridge<sup>2</sup>, Steve H.L.**  
6 **Yim<sup>4,5,6</sup>, Hugh Coe<sup>7</sup>, Suresh Babu<sup>8</sup>, Sreedharan K. Satheesh<sup>9</sup>, Paquita**  
7 **Zuidema<sup>10</sup>, Tao Huang<sup>4</sup>, Jack C.H. Cheng<sup>4</sup>.**

8

9 **Affiliations:**

10 <sup>1</sup>College of Engineering Mathematics, and Physical Sciences, University  
11 of Exeter, Exeter, Devon, UK

12 <sup>2</sup>Met Office, Fitzroy Road, Exeter, Devon, UK

13 <sup>3</sup>College of Life and Environmental Sciences, University of Exeter, Penryn,  
14 Cornwall, UK

15 <sup>4</sup>Department of Geography and Resource Management, The Chinese  
16 University of Hong Kong, Hong Kong, China

17 <sup>5</sup>Stanley Ho Big Data Decision Analytics Research Centre, The Chinese  
18 University of Hong Kong, Hong Kong, China

19 <sup>6</sup>Institute of Environment, Energy and Sustainability, The Chinese  
20 University of Hong Kong, Hong Kong, China



21 <sup>7</sup>Department of Earth and Environmental Sciences, University of  
22 Manchester, Manchester, UK

23 <sup>8</sup>Space Physics Laboratory, Vikram Sarabhai Space Centre, Trivandrum,  
24 695 022, India

25 <sup>9</sup>Centre for Atmospheric and Oceanic Sciences, Indian Institute of Science,  
26 Bangalore 560 012, India

27 <sup>10</sup>Rosenstiel School of Marine and Atmospheric Science, University of  
28 Miami, Miami, FL, USA

29 *Correspondence to:* J. Haywood (J.M.Haywood@exeter.ac.uk)

30 **Abstract:**

31 The Printed Optical Particle Spectrometer (POPS) is an advanced and small low-cost,  
32 light-weight, and high-sensitivity optical particle counter (OPC), particularly designed  
33 for deployed on unpiloted aerial vehicles (UAVs) and balloon sondes. We report the  
34 performance of the POPS against a reference scanning mobility particle sizer (SMPS)  
35 and an airborne passive cavity aerosol spectrometer probe (PCASP) while the POPS is  
36 operated on the ground and also while operated on a quadcopter drone, a DJI Matrice  
37 200 V2. This is the first such documented test of the performance of a POPS instrument  
38 on a UAV. We investigate the root mean square difference (RMSD) and mean absolute  
39 difference (MAD) in particle number concentrations (PNCs) when operating on the  
40 ground and on the Matrice 200. When windspeeds are less than 2.6m/s, we find only  
41 modest differences in the RMSDs and MADs of 2.4% and 2.3% respectively when  
42 operating on the ground, and to 5% and 3% when operating at 10m altitude. When  
43 windspeeds are greater than 2.6m/s but less than 7.7m/s the RMSDs and MADs  
44 increase to 10.2% and 7.8% respectively when operating on the ground, and 26.2% and



45 19.1%, respectively when operating at 10m altitude. No statistical difference in PNCs  
46 was detected when operating on the UAV in either ascent or descent. We also find size  
47 distributions of aerosols in the accumulation mode (here defined by diameter,  $d$ , where  
48  $0.1 \leq d \leq 1\mu\text{m}$ ) are relatively consistent between measurements at the surface and  
49 measurements at 10m altitude with RMSD and MAD of less than 21.6% and 15.7%,  
50 respectively. However, the differences between coarse mode (here defined by  $d > 1\mu\text{m}$ )  
51 are universally larger than those measured at the surface with a RMSD and MAD  
52 approaching 49.5% and 40.4%. Our results suggest that the impact of the UAV rotors  
53 on the POPS does not unduly affect the performance of the POPS for wind speed less  
54 than 2.6m/s, but when operating under higher wind speed of up to 7.6m/s, larger  
55 discrepancies are noted. In addition to this, it appears that the POPS measures sub-  
56 micron aerosol particles more accurately than super-micron aerosol particles when  
57 airborne on the UAV. These measurements lay the foundations for determining the  
58 magnitude of potential errors that might be introduced into measured aerosol particle  
59 size distributions and concentrations owing to the turbulence created by the rotors on  
60 the UAV.

## 61 **1 Introduction**

62 Atmospheric aerosols have a significant impact on Earth's climate as they affect the  
63 radiative balance of the Earth-Atmosphere system through the direct and indirect effect  
64 (e.g. Haywood and Boucher, 2000; Boucher et al., 2013). The direct effect refers to  
65 absorption and scattering of solar and terrestrial radiation by aerosols, and the indirect  
66 effect refers to the ability of aerosols acting as condensation nuclei (CCN), thereby  
67 influencing cloud microphysical properties (Twomey, 1977), and potentially cloud  
68 extent and lifetime (Albrecht, 1989; Haywood and Boucher, 2000). Although there has  
69 been considerable progress in the knowledge and understanding of aerosol physical and



70 chemical properties over the past few decades, estimates of aerosol effects of mean  
71 climate impacts and extreme climatic events remain uncertain (Boucher et al., 2013;  
72 Liu et al., 2019a, b). The size, chemical composition, morphology, and number  
73 concentration of aerosols are all important factors in determining their ability to act as  
74 CCN and in their ability to scatter and absorb solar and terrestrial radiation. Aerosol  
75 concentration and their intrinsic properties are spatially inhomogeneous owing to  
76 different emission sources, deposition processes, transports, and chemical reactions (e.g.  
77 Bellouin et al., 2005; Jiminez et al., 2009; Lack and Cappa, 2010; Atkinson et al., 2018;  
78 Yim et al., 2019; Yim et al., 2020). Among these properties, particle size distributions  
79 (PSDs) and number concentrations (PNCs) are of fundamental importance in  
80 determining the impact of aerosols on the atmospheric radiation budget via the aerosol  
81 direct and indirect effects. Based on observations of the size distributions of aerosols  
82 and aerosol refractive index, aerosol optical properties can be inferred (e.g. Atkinson et  
83 al., 2015). The size of aerosol particles is also of primary importance in cloud formation  
84 and precipitation (Yin et al., 2000; Liu et al., 2018; 2019a). As a result, in order to better  
85 understand the effect of aerosols on climate change, it is important to obtain a  
86 comprehensive and accurate characterization of the spatial distribution of aerosol  
87 concentration and properties. Aerosols also play an important role in atmospheric  
88 visibility (e.g. Horvath, 1981), and in respiratory irritants as they are known to have an  
89 adverse impact on air quality and health (e.g. Li et al., 2003; Gu et al., 2016; 2018;  
90 2020; Shi et al., 2019). In terms of scales, satellite observations (e.g. Bellouin et al.,  
91 2005) are able to provide near global coverage of aerosol optical depths, but are only



92 able to provide bulk measurements of properties of the aerosol size distribution (e.g.  
93 fine mode fraction) and aerosol optical properties (e.g. aerosol absorption). Dedicated  
94 field sites (e.g. Zuidema et al., 2016, 2018) or dedicated sampling with aircraft  
95 instrumentation (e.g. Haywood et al., 2003a; 2020) are able to make much more  
96 detailed aerosol microphysical measurements, but are costly and aircraft cannot sample  
97 aerosols at low altitude in built-up urban regions owing to obvious safety concerns. The  
98 atmospheric science community frequently utilizes optical particle counters (OPCs)  
99 and Mie scattering theory for sizing individual aerosol particles (e.g. Burkhardt et al.,  
100 2010). Measurements of aerosols by small, unmanned aerial vehicles (UAVs) have  
101 many advantages, such as low-cost, ease and cost of deployment, and ease of access to  
102 inaccessible areas such as those close to urban conurbations. However, owing to  
103 payload restrictions, UAVs require light-weight, minaturized OPCs. The Printed  
104 Optical Particle Spectrometer (POPS) is an advanced and small low-cost, light-weight,  
105 and high-sensitivity OPC, particularly designed for UAVs and balloon sondes (Gao et  
106 al., 2013; 2016). In brief, the POPS samples particles by drawing air through an inlet  
107 tube into an optical chamber, where it is illuminated by a 405nm laser. A sheath air  
108 flow is used to focus the sample air into the centre of the laser beam, and the sample  
109 flow is maintained at a near constant rate by an automatically regulated on-board pump.  
110 Scattered laser light is reflected into a photomultiplier tube by a hemispherical mirror,  
111 and the signal amplitude recorded by a data logger. Individual particle sizes are then  
112 inferred by comparing the recorded signal amplitudes to scattering amplitudes  
113 calculated using Mie scattering theory.



114 The POPS has been carried by balloon sondes to study the vertical profile of the Asian  
115 Tropopause Aerosol Layer (Yu et al., 2017), but quantitative data when deployed on a  
116 quadcopter drone is very sparse. There have been some recent side-by-side tests of  
117 miniaturized OPC instruments against more established instrumentation in controlled  
118 environments (e.g. Bezantakos et al., 2018), and some limited comparisons against  
119 large atmospheric tower based instrumentation (Ahn, 2019). A significant question  
120 related to deploying the POPS instrument on a quadcopter drone is whether the  
121 turbulence generated by the multiple rotors impacts the measurements of the aerosol  
122 concentrations and size distributions, and if so, to what extent. Here we provide the first  
123 comprehensive documentation of the performance of the POPS on a multi-rotor UAV.  
124 We first investigated the performance of the POPS instrument in a closely controlled  
125 environment on the ground in a three-week comparison of the POPS against reference  
126 instruments. The POPS was deployed at the Atmospheric Radiation Measurements  
127 (ARM) mobile facility on Ascension Island during colocation of the Layered Atlantic  
128 Smoke Interaction with Clouds (LASIC; Zuidema et al., 2016) and CLOUD-Aerosol-  
129 Radiation Interaction and Forcing: Year-2017 (CLARIFY-2017; Haywood et al., 2020)  
130 measurement campaigns. Subsequently we examined the influence of the rotors from  
131 the drone on the measured aerosol number concentration and size distribution. Section  
132 2 presents the methodology used in the ground-based comparison and the UAV-  
133 mounted flights, section 3 presents the results before conclusions and future work is  
134 presented in section 4.



## 135 **2 Methods**

### 136 **2.1 A 20-day comparison**

137 As part of the CLARIFY-2017 and LASIC campaign, the POPS was deployed at the  
138 ARM mobile site on Ascension Island located in the mid-Atlantic ( $-7.96^{\circ}$  N,  $-14.37^{\circ}$  E)  
139 alongside an ARM operated SMPS. The time period for sampling for both instruments  
140 analyzed here was from 20th August to 9th September 2017 (20 days) continuously,  
141 during which time biomass burning aerosol originating from the African continent was  
142 frequently present (Zuidema et al., 2018; Haywood, 2020). The SMPS and the POPS  
143 were connected to a common aerosol inlet, however, in the case of the SMPS, the  
144 sample air was dried before it entered the instrument.

145  
146 In common with other OPCs, the POPS size distributions are influenced by the  
147 refractive index assumed in the Mie calculations. The manufacturer (Handix Scientific)  
148 provides a calibration for the POPS using well-sized latex spheres with a refractive  
149 index (RI) of  $1.615+0.001i$  at 405 nm. Prior to deployment to Ascension Island, the  
150 manufacturer's calibration of the POPS was adjusted through independent lab-based  
151 measurements using latex spheres at the UK's Facility for Airborne Atmospheric  
152 Research (FAAM, <https://www.faam.ac.uk/>). Errors in the PSDs can be caused by  
153 sampling aerosols with a different refractive index, particularly if they are significantly  
154 absorbing (e.g. Haywood et al., 2003). The independent lab-based calibrations were  
155 therefore adjusted assuming a RI of  $1.54+0.027i$  at 405 nm, which is expected to be  
156 more representative of the biomass burning aerosol particles sampled at the ARM site



157 during the CLARIFY deployment (Peers et al., 2019). In the test flights determining  
158 the impact of rotors, the RI of  $1.54+0.027i$  was also applied as it is the relative  
159 difference in the size distribution and concentration that are of most concern during  
160 those operating periods. Compared with the POPS, the SMPS that was operated by the  
161 ARM mobile Facility uses particle mobility subsequent to application of an electrostatic  
162 charge to size aerosol particles, a method which is independent of the refractive index  
163 (Ruzer and Harley, 2012).

164

165 In addition to applying fundamentally different methods to measure the size of particles,  
166 the POPS and SMPS cover different ranges of size distributions. The POPS measures  
167 particles within the diameter range from around  $0.12 - 4.44\mu\text{m}$  (for  $\text{RI} = 1.54+0.027i$   
168 at  $405\text{ nm}$ ), while the SMPS covers diameter ranging from around  $0.01$  to  $1.00\mu\text{m}$ .

## 169 **2.2 Drone-mounted POPS**

170 The POPS required a carefully designed bespoke rig to fit it safely to a quadcopter  
171 drone for deployment. A DJI Matrice 200 V2 was used because it had a sufficient power  
172 and payload capacity to lift the POPS and even with the relatively high payload could  
173 offer reasonable endurance. The maximum flight time of the Matrice is 24 minutes with  
174 the maximum payload ( $1.45\text{kg}$ ). University of Exeter and Met Office staff designed and  
175 fitted the POPS to the Matrice airframe (Figure 1). The POPS was installed at the  
176 bottom left of the fuselage and fixed on the customized 3-D printed landing gear. The  
177 inlet tube of the POPS (red oval in Figure 1) reached  $20\text{cm}$  above the rotors. The



178 diameter of the inlet tube is 1mm and the sample flow rate is 3 cm<sup>3</sup>/s, yielding a flow  
179 velocity of 3.8m/s. No attempt has been made to optimise this simple tube inlet for  
180 drone applications. The data were collected during 14 test flights in total from 18<sup>th</sup>  
181 December 2019 to 9<sup>th</sup> March 2020 to determine any impact of the rotors on the data  
182 from the POPS. Each test flight was planned to be separated into three stages. During  
183 the first stage, the drone was on the ground with the rotors off for ten minutes (G\_NR).  
184 In the second stage, the drone was on the ground with the rotors on for the next ten  
185 minutes (G\_R). In the last stage the drone hovered at a fixed position and fixed altitude  
186 of ten meters above the surface for ten minutes (FLY). A summary of date and time of  
187 each test flight is given in Table 1. There are some deviations from the G\_NR, G\_R and  
188 FLY routines. T1 was a pre-test so there was no FLY. Additionally, due to high wind  
189 speeds and associated operational safety concerns, T9 and T13 had to reduce the test  
190 time of FLY to 7 minutes and 5 minutes, respectively. Three vertical profiles were made  
191 at the end of T10, T12, and T13, the details of which are provided in Table 2. The main  
192 purpose of profiling during T10, T12 and T13 was to investigate: 1) the stability in the  
193 POPS instrument when profiling up and down as this is likely to be a prime operating  
194 maneuver when flying scientific sorties in the future; 2) the performance of the POPS  
195 at different vertical ascent and descent rates; and 3) the accuracy of the POPS on the  
196 way up and way down which could conceivably be influenced by turbulent disturbance  
197 by the rotors, particularly on vertical descents when the aerosol inlet will be in the wake  
198 of the drone rotors. The test flights were all performed at the Streatham campus of the  
199 University of Exeter (50.73N, 3.53W), UK.



## 200 **3 Results**

### 201 **3.1 Comparison of POPS data against data from** 202 **LASIC/CLARIFY-2017.**

203 Figure 2 shows the mean PSD measured by the POPS and SMPS for the 20-day period,  
204 respectively. Figure 2 represents the whole size range of the two instruments as well as  
205 the fitted PSD from measurements with a wing-mounted PCASP-100X mounted on the  
206 UK's Bae146 FAAM aircraft from a flight during CLARIFY-2017 (Peers et al., 2019),  
207 which has been shown to be representative of biomass burning aerosol during the wider  
208 CLARIFY-2017 measurement campaign (Wu et al., 2020). That the POPS and SMPS  
209 show close overlap at the peak concentrations indicates that the counting statistics and  
210 the particle concentrations are similar between the instruments. The mean PSD  
211 measured by the POPS and SMPS shows reasonable agreement. Although the  
212 agreement is not as good as that demonstrated in other comparisons against SMPS  
213 instruments (e.g. Gao et al., 2016), any resulting errors in derived optical parameters  
214 are likely to be small provided the fit is reasonable over the 0.2-1.0  $\mu\text{m}$  diameter range.  
215 Measurements of biomass burning aerosol over the Atlantic from the SAFARI-2000  
216 campaign suggest that particles in this range contribute to 93% of the scattering at  
217 0.55 $\mu\text{m}$  (e.g. Table 1, Haywood et al., 2003). The PSD from the wing-borne PCASP-  
218 100X that was operated on the FAAM bears a close resemblance to the SMPS and  
219 POPS PSDs except at particle sizes  $<0.2\mu\text{m}$  diameter and  $>0.7\mu\text{m}$  diameter. The  
220 discrepancy at particle sizes  $<0.2\mu\text{m}$  might be expected because the fits that are adopted



221 by Haywood et al. (2003) and Peers et al. (2019) do not account for these small particles  
222 as they were developed with simplicity in mind for global general circulation models  
223 of aerosol optical properties and for satellite retrievals respectively. Examination of the  
224 PCASP data to which the log-normal distributions were fitted from both the CLARIFY-  
225 2017 and SAFARI-2000 data indicates higher concentrations of aerosol at these small  
226 sizes than the log-normal fits can represent. Aerosols  $>0.7\mu\text{m}$  diameter that were  
227 observed by the POPS that were not present in the CLARIFY-2017 or SAFARI-2000  
228 data may well be generated by dust generation from the arid surface of Ascension Island  
229 or by super-micron sea-salt from breaking waves. Taylor et al (2020) document the  
230 enhanced influence of the oceanic component of aerosols in the marine boundary layer,  
231 but this is not included in the CLARIFY-2017 or SAFARI-2000 log-normal fits which  
232 represent biomass burning aerosols only. Thus, the POPS instrument appears to provide  
233 a reasonably quantitative measure of optically active sub-micron aerosols.

234

235 We also investigated the overall particle number concentration from the POPS, and  
236 examine the time series of the POPS measurements against some other key variables  
237 measured by the SMPS and other instrumentation at the ARM mobile facility. The  
238 upper panel of Figure 3a presents the 20-day intercomparison of the PNCs from the  
239 POPS and SMPS, and panel 3b shows the ratio of the two concentration measurements  
240 (POPS/SMPS). They show a good agreement between two instruments while the  
241 geometric mean diameter (GMD) the of the size distribution (Figure 3c) is above



242 0.12 $\mu$ m. Again, this illustrates that the POPS instrument measures accumulation mode  
243 aerosols reasonably accurately.

244

245 We would expect biomass burning aerosols to be associated with an increase in carbon  
246 monoxide (CO; Haywood et al., 2003; Wu et al., 2020), and the concentrations  
247 measured by both the POPS and SMPS instruments are well correlated with the CO  
248 mass mixing ratio (as measured by a co-located CO analyzer – Figure 3d). The  
249 concentration data also show some correlation with the AODs as measured by a co-  
250 located AERONET Cimel sun-photometer (panel five, Figure 3), although this AOD is  
251 a column measurement rather than a point measurement so the influence of vertical  
252 profile will likely be important (e.g. Wu et al, 2020; Haywood et al, 2020).

### 253 **3.2 Test flight results**

254 To determine the impact of rotors on the POPS, we focus on the comparison of PSD  
255 and PNC at three different stages: G\_NR, G\_R, and FLY. Table 3 summaries the mean  
256 PNC with standard deviation and the PNC percentage differences of each flight at  
257 different stages.

#### 258 3.2.1. Particle number concentration (PNC)

259 Compared with the mean PNC at G\_NR, the mean PNC at G\_R changed from -1% to  
260 26%, and that at FLY changed from -1% to 63%, respectively. However, it is apparent  
261 that the differences of PNCs are much lower in the cases T1, T2, T6, T7, and T10 (less  
262 than 10%) in both stages. Figure 4 shows the probability density functions of PNC in



263 each case. The PNC at three stages of each case were separated into 15 bins. Unpaired  
264 two-sample t-tests were selected to detect the similarity of the PNCs at different stages  
265 as the t-test is the most popular parametric test for samples following normal  
266 distribution for calculating the significance of a small sample size (De Winter, 2013).  
267 Here the PNC of G\_NR was set as the control group, while that of G\_R and FLY was  
268 set as the perturbation groups using the mean PNC at each stage every 30 seconds.  
269 Before the t-test, the Levene's test was performed which is an inferential statistic used  
270 to assess the equality of variances for a variable calculated for two or more groups  
271 (Levene, 1960). If the Levene's test cannot be passed, then the unequal variances t-test,  
272 which is a more conservative test, was be applied for the groups. The results (p value)  
273 of the t-test of each test flight are shown in Table 4.  
274  
275 For a significance level ( $\alpha$ ) set as 0.05, there are 5 test flights that passed the t test in  
276 both G\_R and FLY stages ( $p \text{ value} \geq \alpha$ ), which means the PNC measured at G\_R and  
277 FLY stage corresponded well with those measured at G\_NR. These test numbers have  
278 been marked in green and bold italic font in Table 4. This result indicates that the impact  
279 of rotors was not significant in these five cases. The other three cases (T8, T9, and T14)  
280 passed the t-test in the G\_R stage, which are marked yellow and italic font. The rest of  
281 test flights did not pass the t-test in either stage (marked red and standard font). Through  
282 comparing the weather conditions, we find that the wind speed (Table 4) was relatively  
283 lower (0.5-2.6m/s) in the cases which pass the t-test at both stages. The wind speed in  
284 the Table 4 was provided from observations at Exeter airport with one-hour resolution.  
285 During the actual experiment, when the wind speed was high, visual observations by



286 the drone pilot suggested that the drone swung from side to side in the air, causing  
287 increased variability in the pitch, yaw and altitude of the drone. As previously noted,  
288 on T9 and T13 the drone was forced to land early to ensure safety due to the high (>7  
289 m/s) instantaneous wind speed.

290

291 To determine the impact of wind speed on PNC observed by the POPS, the cases are  
292 separated into 2 categories: low wind speed ( $w < 2.6$  m/s) cases and high wind speed  
293 ( $2.6 < w < 7.7$  m/s) cases. The PNC root mean square differences (RMSD) and mean  
294 absolute differences (MAD) at G\_R and FLY for all cases, low wind speed cases, and  
295 high wind speed cases are given in the Table 5. For all cases, PNC RMSD is less than  
296 10.2% at G\_R and less than 26.2% at FLY, and MAD is less than 7.8% at G\_R and less  
297 than 19.1% at FLY. However, in the low wind cases, the RMSD and MAD fall to 2.4%  
298 and 2.3% at G\_R, and 5% and 3% at FLY, respectively. In contrast, RMSD and MAD  
299 in the high wind cases increase to 12.6% and 10.9% at G\_R, 31.4% and 26.3% at FLY,  
300 respectively. Thus it appears that the inlet air flow of the POPS was not stable when the  
301 drone suffered from variations in pitch and yaw under high wind speed conditions,  
302 which leads to significant fluctuation and variability of the PNC recorded by the POPS  
303 at high wind speed.

304

305 3.2.2. The particle size distribution (PSD)

306 The PSDs at different stages and the mean PSDs ratios at G\_R to G\_NR and FLY to  
307 G\_NR of each test flight are shown in Figure 5, which indicates that the cases with high



308 similarity of PNCs (T1, T2, T6, T7, and T10) show agreement of the PSD. It also shows  
309 that the differences of sub-micron sizes are less than those of super-micron sizes at G\_R  
310 and FLY. Therefore, the size distribution was separated into two modes, the  
311 accumulation mode ( $0.1 \leq d \leq 1.0\mu\text{m}$ ) and the coarse mode ( $d > 1.0\mu\text{m}$ ), to make a  
312 statistical analysis. Table 6 summaries the PSDs percentage differences for two modes  
313 at G\_R and FLY for each case. The PSDs RMSD and MAD for two modes at G\_R and  
314 FLY for all cases, low wind cases, and high wind cases are given in Table 6. The  
315 percentage differences of the PSDs are less than 5.4% and 14.9% in low wind cases at  
316 the accumulation mode at G\_R and FLY, respectively, while the variation in the PSD in  
317 the coarse mode is perhaps due to lower counting statistics at these sizes. In contrast  
318 PSDs of other cases show differences across the whole spectrum. Even in the  
319 accumulation mode, the differences of the PSDs between FLY and G\_NR are up to 53.2%  
320 in the case T8. PSDs RMSD and MAD at the accumulation mode are 3.4% and 2.7%  
321 respectively at G\_R in the low wind speed cases, but up to 12.9% and 11.1% at G\_R in  
322 the high wind speed cases. These statistics again indicate that impacts of rotors and  
323 UAV attitude on the POPS measurements appear to be reduced in low wind speeds  
324 relative to higher wind speeds. PSD RMSDs and MADs at the coarse mode at G\_R,  
325 and at the accumulation and coarse mode at FLY show the same result. Generally  
326 speaking, RMSDs and MADs indicate the impact of rotors and UAV attitude on the  
327 POPS operated in accumulation mode is lower than when in coarse mode, for all cases.  
328 RMSDs in accumulation mode were 10.6% at G\_R and 21.6% at FLY, while those in  
329 coarse mode were 32.2% and 49.5% for all cases. MADs showed the same trend as



330 RMSDs. In the absence of independent multi-stage meteorological tower  
331 measurements (e.g. Ahn, 2019), it is difficult to assess how much of the variability in  
332 PNCs and PSDs is real, particularly when the drone is flying; there may be changes in  
333 PNC with altitude when compared to the surface PNCs owing to surface deposition.  
334 Alternatively, there may be trends in the particle concentrations that occur during the  
335 entire measurement period. A potential solution to the latter would be to change the  
336 three stage sequence from G\_NR, G\_R, FLY to a five stage sequence of G\_NR, and  
337 G\_NR. This sequence is suggested for future investigations.

338

### 339 3.2.3. The PNC during vertical profiles

340 Figure 6 presents the results of the vertical profile runs in T10, T12, and T13. The mean  
341 PNC with standard deviation on the way up and down are shown in Table 7. The PNC  
342 measured on the way up and way down show agreement. The best agreement is found  
343 in the high number concentration, low wind-speed case (T10), where the PNCs differ  
344 by an average of 0.5% between ascent and descent. Even in the high wind-speed cases  
345 when the variability might be expected to be largest owing to changes in the pitch and  
346 yaw of the drone, general agreement is found indicating that the vertical speed of the  
347 drone (which was approximately 0.5 to 1m/s) does not appear to have a significant  
348 impact. Note that the vertical profiles do indicate some variability in the vertical  
349 distribution with PNCs ranging from  $1207 \pm 83 \text{ cm}^{-3}$ ,  $69 \pm 14 \text{ cm}^{-3}$ , and  $90 \pm 11 \text{ cm}^{-3}$  close to  
350 the surface to  $1189 \pm 107 \text{ cm}^{-3}$ ,  $55 \pm 11 \text{ cm}^{-3}$ , and  $72 \pm 15 \text{ cm}^{-3}$  in ascent and  $1395 \pm 83 \text{ cm}^{-3}$ ,  
351  $69 \pm 5 \text{ cm}^{-3}$ , and  $89 \pm 6 \text{ cm}^{-3}$  close to the surface to  $1201 \pm 101 \text{ cm}^{-3}$ ,  $54 \pm 12 \text{ cm}^{-3}$ , and  $82 \pm 13$   
352  $\text{cm}^{-3}$  in descent for flights T10, T12 and T13. This variability with height emphasizes



353 the utility of small, instrumented UAVs for measuring PNCs and PSDs at low altitudes;  
354 measurements at such altitudes are impossible to probe with heavily equipped  
355 atmospheric research aircraft operating under standard aviation safety protocols.

## 356 **4 Conclusions**

357 We have investigated the performance of POPS against a reference SMPS instrument  
358 while on the ground and also while operated on a quadcopter drone, DJI Matrice 200  
359 V2, which is the first documented test of the performance of a POPS instrument on a  
360 UAV. The investigation includes two parts. The first is a long-term comparison between  
361 the POPS and other instruments during the CLARIFY-2017/LASIC and SAFARI-2000  
362 project. The results show that the PNC measured by the POPS and that measured by  
363 the SMPS and PCASP indicate agreement in the optically important size range centred  
364 at around  $0.3\mu\text{m}$  diameter. This indicates that despite its small size, when operating  
365 under controlled conditions on the ground, the POPS instrument performs relatively  
366 well. In the second part, we tested the impact of drone's rotors and, indirectly the  
367 attitude of the drone, on the performance of the POPS with a focus on two aspects, the  
368 PNC and PSD. We found RMSDs and MADs in PNC when operating a POPS on a  
369 small quad-copter to be less than 10.2% and 7.8%, respectively, when operating on the  
370 ground, and less than 26.2% and 19.1%, respectively, at 10m altitude under wind speed  
371 conditions of up to 7.7m/s. For wind speed of less than 2.6m/s, RMSDs and MADs fell  
372 to 2.4% and 2.3% when operating on the ground, and to 5% and 3% at 10m altitude.  
373 We also found no statistical difference in PNC when operating the UAV in either ascent



374 or descent. As for the PSD, the accumulation mode aerosol size distributions were  
375 relatively invariant between measurements at the surface and measurements at 10m  
376 altitude with RMSD and MAD of less than 21.6% and 15.7%, respectively. The  
377 differences between coarse mode super-micron aerosols measured at the surface and at  
378 10m altitude were universally greater than those measured at the surface with a RMSD  
379 and MAD approaching 49.5% and 40.4%, but it is unclear whether this is due to loss  
380 of coarse mode aerosol particles to the surface or whether this is due to interference  
381 from the rotors. This impact appears to be most prevalent at the larger end of the POPS  
382 size range. These results suggest that the POPS and UAV and very simple inlet  
383 combination examined here appears able to measure the aerosol PSD and PNC with  
384 reasonable fidelity, particularly for sub-micron aerosols when the wind-speed is  
385 relatively modest.

386

387 In follow-up scientific observations, the POPS deployed on the quadcopter drone will  
388 be used to measure the aerosol properties in the atmospheric boundary layer (ABL)  
389 under polluted condition. Concentration of pollutants in the ABL frequently have a  
390 strong correlation with atmospheric stability (Wang et al., 2013, Chambers et al., 2015)  
391 with stable conditions leading to the build-up of pollutants in the ABL. Wind-speeds  
392 are frequently low in stable conditions due to the lack of convection driven turbulence.  
393 Because these future measurements are likely under stable, non-turbulent conditions,  
394 wind-speed effects are not likely to cause significant problems. For other applications  
395 of the POPS on a quadcopter drone, such as the dispersion of pollutants in down-wind



396 driven plumes, attention should be paid to the influence of the higher wind speeds.

397 **Acknowledgements:** This work was supported by the Chinese University of Hong  
398 Kong – University of Exeter Joint Centre for ENvironmental SUstainability and  
399 REsilience (ENSURE) programme; ZL, MO, JH, KA, JS, TH, JC and SY would like  
400 to thank ENSURE for their financial support. JH, ZL and HC would also like to  
401 acknowledge NERC SWAAMI (South West Asian Aerosol Monsoon Interactions)  
402 grants NE/L013878/1 and NE/L013886/1 for partial funding of the research.

403

404

405

406

407

408

409

410

411

412

413

414

415

416

417



## 418 References

- 419 Ahn, K-H, Aerosol 3D Profiling Using Compact Particle Measuring Instruments with Balloon  
420 and Drone System, *7th International Symposium on Ultrafine Particles, Air Quality and*  
421 *Climate (2019)*, DOI: 10.5445/IR/1000096749,
- 422 Albrecht, B. A. (1989). Aerosols, cloud microphysics, and fractional cloudiness. *Science*,  
423 245(4923), 1227-1230.
- 424 Atkinson, D. B., Pekour, M., Chand, D., Radney, J. G., Kolesar, K. R., Zhang, Q., Setyan, A.,  
425 O'Neill, N. T. & Cappa, C. D. 2018. Using spectral methods to obtain particle size  
426 information from optical data: applications to measurements from CARES 2010.  
427 *Atmospheric Chemistry and Physics*, 18, 5499-5514.
- 428 Atkinson, D. B., Radney, J. G., Lum, J., Kolesar, K. R., Cziczo, D. J., Pekour, M., Zhang, Q.,  
429 Setyan, A., Zelenyuk, A. & Cappa, C. D. 2015. Aerosol optical hygroscopicity  
430 measurements during the 2010 CARES campaign. *Atmospheric Chemistry and*  
431 *Physics*, 15, 4045–4061.
- 432 Bellouin, N., Boucher, O., Haywood, J., & Reddy, M. S. (2005). Global estimate of aerosol direct  
433 radiative forcing from satellite measurements. *Nature*, 438(7071), 1138-1141.
- 434 Boucher, O., D. Randall, P. Artaxo, C. Bretherton, G. Feingold, P. Forster, V.-M. Kerminen, Y.  
435 Kondo, H. Liao, U. Lohmann, P. Rasch, S.K. Satheesh, S. Sherwood, B. Stevens and  
436 X.Y. Zhang, 2013: Clouds and Aerosols. In: *Climate Change 2013: The Physical*  
437 *Science Basis. Contribution of Working Group I to the Fifth Assessment Report of the*  
438 *Intergovernmental Panel on Climate Change [Stocker, T.F., D. Qin, G.-K. Plattner, M.*  
439 *Tignor, S.K. Allen, J. Boschung, A. Nauels, Y. Xia, V. Bex and P.M. Midgley (eds.)].*  
440 *Cambridge University Press, Cambridge, United Kingdom and New York, NY, USA.*
- 441 Burkart, J., Steiner, G., Reischl, G., Moshhammer, H., Neuberger, M., & Hitzenberger, R. (2010).  
442 Characterizing the performance of two optical particle counters (Grimm OPC1. 108 and  
443 OPC1. 109) under urban aerosol conditions. *Journal of Aerosol Science*, 41(10), 953-  
444 962.
- 445 Chambers, S. D., Wang, F., Williams, A. G., Xiaodong, D., Zhang, H., Lonati, G., Crawford, J.,  
446 Griffiths, A. D., Ianniello, A. & Allegrini, I. 2015. Quantifying the influences of  
447 atmospheric stability on air pollution in Lanzhou, China, using a radon-based stability  
448 monitor. *Atmospheric Environment*, 107, 233-243.
- 449 De Winter, J. C. 2013. Using the Student's t-test with extremely small sample sizes. *Practical*  
450 *Assessment, Research, and Evaluation*, 18, 10.
- 451 Gao, R., Perring, A., Thornberry, T., Rollins, A., Schwarz, J., Ciciora, S. & Fahey, D. 2013. A  
452 high-sensitivity low-cost optical particle counter design. *Aerosol Science and*  
453 *Technology*, 47, 137-145.
- 454 Gao, R., Telg, H., McLaughlin, R., Ciciora, S., Watts, L., Richardson, M., Schwarz, J., Perring,  
455 A., Thornberry, T. & Rollins, A. 2016. A light-weight, high-sensitivity particle  
456 spectrometer for PM<sub>2.5</sub> aerosol measurements. *Aerosol Science and Technology*, 50,  
457 88-99.
- 458 Gu Y. and Yim S.H.L. (2016). The air quality and health impacts of domestic trans-boundary  
459 pollution in various regions of China. *Environment International*, 97, 117-124.
- 460 Gu Y., Wong T.W., Law S.C.K., Dong G.H., Ho K.F., Yang Y., Yim S.H.L. (2018). Impacts of



- 461 Sectoral Emissions in China and the Implications: Air Quality, Public Health, Crop  
462 Production, and Economic Costs. *Environmental Research Letters*, 13, 8.
- 463 Gu Y., Zhang W., Yang Y., Wang C., Streets D.G., Yim S.H.L. (2020). Assessing outdoor air  
464 quality and public health impact attributable to residential black carbon emissions in  
465 rural China. *Resources, Conservation and Recycling*, 159, 104812.
- 466 Haywood, J., & Boucher, O. (2000). Estimates of the direct and indirect radiative forcing due to  
467 tropospheric aerosols: A review. *Reviews of geophysics*, 38(4), 513-543.
- 468 Haywood, J., Francis, P., Dubovik, O., Glew, M. & Holben, B. 2003a. Comparison of aerosol  
469 size distributions, radiative properties, and optical depths determined by aircraft  
470 observations and Sun photometers during SAFARI 2000. *Journal of Geophysical  
471 Research: Atmospheres*, 108.
- 472 Haywood, J. M., Osborne, S. R., Francis, P. N., Keil, A., Formenti, P., Andreae, M. O. & Kaye,  
473 P. H. 2003b. The mean physical and optical properties of regional haze dominated by  
474 biomass burning aerosol measured from the C-130 aircraft during SAFARI 2000.  
475 *Journal of Geophysical Research: Atmospheres*, 108.
- 476 Haywood, J.M., S. J. Abel, P. Barrett, N. Bellouin, A. Blyth, K.N. Bower, M. Brooks, K. Carslaw,  
477 H. Coe, M. Cotterell, I. Crawford, N. Davies, B. Dingley, P. Field, P. Formenti, H. Gordon,  
478 M. de Graaf, R. Herbert, B. Johnson, A.C. Jones, F. Malavelle, D.G. Partridge, F. Peers,  
479 J. Redemann, P. Stier, J. Taylor, R. Wood, H.H. Wu, P. Zuidema. Overview of the  
480 CLOUD-Aerosol-Radiation Interaction and Forcing: Year-2017 (CLARIFY-2017)  
481 measurement campaign, acp-2020-729, *Atmos Chem Phys Diss*, 2020.
- 482 Horvath, H. (1981). Atmospheric visibility. *Atmospheric Environment* (1967), 15(10-11), 1785-  
483 1796.
- 484 IPCC: Climate Change 2013: The Physical Science Basis. Contribution of Working Group I to  
485 the Fifth Assessment Report of the Intergovernmental Panel on Climate Change,  
486 Cambridge University Press, Cambridge, United Kingdom and New York, NY, USA, 2013.
- 487 Jimenez, J.L., Canagaratna, M.R., Donahue, N.M., Prevot, A.S.H., Zhang, Q., Kroll, J.H.,  
488 DeCarlo, P.F., Allan, J.D., Coe, H., Ng, N.L. and Aiken, A.C., 2009. Evolution of organic  
489 aerosols in the atmosphere. *Science*, 326(5959), pp.1525-1529.
- 490 Lack, D. & Cappa, C. 2010. Impact of brown and clear carbon on light absorption enhancement,  
491 single scatter albedo and absorption wavelength dependence of black carbon.  
492 *Atmospheric Chemistry and Physics*, 10, 4207.
- 493 Levene, H. 1960. Robust tests for equality of variances. In: *Ingram Olkin, Harold Hotelling, et alia.*  
494 *Contributions to Probability and Statistics: Essays in Honor of Harold Hotelling.*  
495 *Stanford University*, 278-292.
- 496 Li, N. Hao, M. Phalen, R. Hinds, W. and Nel, N. "Particulate air pollutants and asthma: a  
497 paradigm for the role of oxidative stress in PM-induced adverse health effects." *Clinical  
498 immunology* 109, no. 3 (2003): 250-265.
- 499 Liu Z., Ming Y., Zhao C., Lau N.C., Guo J., Bollasina M., Yim S.H.L. (2019a). Contribution of  
500 local and remote anthropogenic aerosols to a record-breaking torrential rainfall event  
501 in Guangdong Province, China. *Atmospheric Chemistry and Physics*, 20, 223-241.
- 502 Liu Z., Ming Y., Wang L., Bollasina M., Luo M., Lau N.C., Yim S.H.L. (2019b). A Model  
503 Investigation of Aerosol-Induced Changes in the East Asian Winter Monsoon.  
504 *Geophysical Research Letters*, 46(16), 10186-10195.



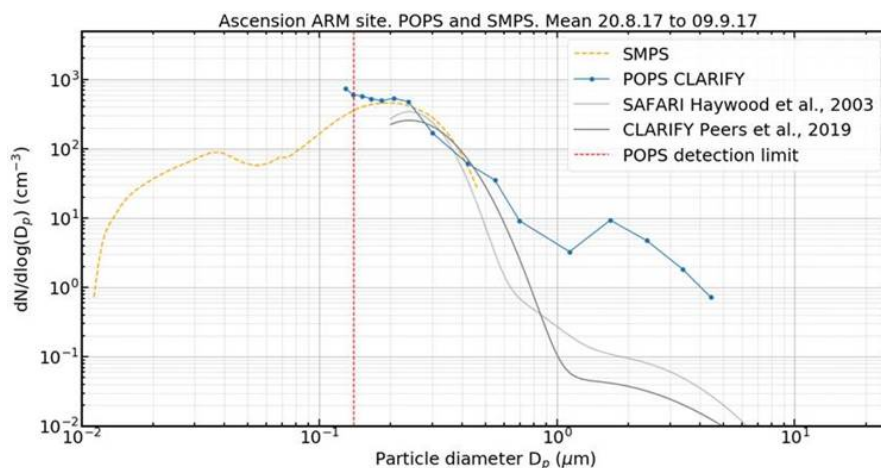
- 505 Liu Z., Yim S.H.L., Wang C., Lau N.C. (2018). The impact of the aerosol direct radiative forcing  
506 on deep convection and air quality in the Pearl River Delta region. *Geophysical*  
507 *Research Letters*, 45(9), 4410-4418.
- 508 Peers, F., Francis, P., Fox, C., Abel, S.J., Szpek, K., Cotterell, M.I., Davies, N.W., Langridge,  
509 J.M., Meyer, K.G., Platnick, S.E. and Haywood, J.M., 2019. Observation of absorbing  
510 aerosols above clouds over the south-east Atlantic Ocean from the geostationary  
511 satellite SEVIRI–Part 1: Method description and sensitivity. *Atmospheric Chemistry and*  
512 *Physics*, 19, 9595–9611, 2019 <https://doi.org/10.5194/acp-19-9595-2019>.
- 513 Ruzer, L. S. & Harley, N. H. 2012. *Aerosols handbook: measurement, dosimetry, and health*  
514 *effects*, CRC press.
- 515 Sang-Nourpour, N., & Olfert, J. S. (2019). Calibration of optical particle counters with an  
516 aerodynamic aerosol classifier. *Journal of Aerosol Science*, 138, 105452.
- 517 Shi C., Nduka I.C., Yang Y., Huang Y., Yao R., Zhang H., He B., Xie C., Wang Z., Yim S.H.L.  
518 (2019). Characteristics and Meteorological Mechanisms of Transboundary Air Pollution  
519 in A Persistent Heavy PM<sub>2.5</sub> Pollution Episode in Central-East China. *Atmospheric*  
520 *Environment*, 223, 117239.
- 521 Taylor, J. W., Wu, H., Szpek, K., Bower, K., Crawford, I., Flynn, M. J., Williams, P. I., Dorsey, J.,  
522 Langridge, J. M., Cotterell, M. I., Fox, C., Davies, N. W., Haywood, J. M., and Coe, H.:  
523 Absorption closure in highly aged biomass burning smoke, *Atmospheric Chemistry and*  
524 *Physics*, 20, 11201–11221, <https://doi.org/10.5194/acp-20-11201-2020>, 2020.
- 525 Twomey, S. (1977). The influence of pollution on the shortwave albedo of clouds. *Journal of the*  
526 *atmospheric sciences*, 34(7), 1149-1152.
- 527 Wang, F., Zang, H., Ancora, M. & Deng, X. 2013. Measurement of atmospheric stability index  
528 by monitoring radon natural radioactivity. *China Environmental Science*, 33, 594-598.
- 529 Wu, H., J.W. Taylor, K. Szpek, P.I. Williams, M. Flynn, J. Langridge, J.D. Allan, J. Pitt, S. Abel,  
530 J. Haywood, H. Coe, Vertical and temporal variability of the properties of transported  
531 biomass burning aerosol over the southeast Atlantic during CLARIFY-2017, *ACPD*.
- 532 Yim S.H.L., Gu Y., Shapiro M., Stephens B. (2019). Air quality and acid deposition impacts of  
533 local emissions and transboundary air pollution in Japan and South Korea. *Atmospheric*  
534 *Chemistry and Physics*, 19, 13309-13323.
- 535 Yim S.H.L. (2020). Development of a 3D Real-Time Atmospheric Monitoring System  
536 (3DREAMS) Using Doppler LiDARs and Applications for Long-Term Analysis and Hot-  
537 and-Polluted Episodes. *Remote Sensing* 12 (6), 1036.
- 538 Yin, Y., Levin, Z., Reisin, T. G. & Tzivion, S. 2000. The effects of giant cloud condensation nuclei  
539 on the development of precipitation in convective clouds—A numerical study.  
540 *Atmospheric Research*, 53, 91-116.
- 541 Yu, P., Rosenlof, K. H., Liu, S., Telg, H., Thornberry, T. D., Rollins, A. W., Portmann, R. W., Bai,  
542 Z., Ray, E. A. & Duan, Y. 2017. Efficient transport of tropospheric aerosol into the  
543 stratosphere via the Asian summer monsoon anticyclone. *Proceedings of the National*  
544 *Academy of Sciences*, 114, 6972-6977.
- 545 Zuidema, P., Sedlacek III, A.J., Flynn, C., Springston, S., Delgadillo, R., Zhang, J., Aiken, A.C.,  
546 Koontz, A. and Muradyan, P., 2018. The Ascension Island boundary layer in the remote  
547 southeast Atlantic is often smoky. *Geophysical Research Letters*, 45(9), pp.4456-4465.
- 548 Zuidema, P., Redemann, J., Haywood, J., Wood, R., Piketh, S., Hipondoka, M. and Formenti,



549 P., 2016. Smoke and clouds above the southeast Atlantic: Upcoming field campaigns  
550 probe absorbing aerosol's impact on climate. *Bulletin of the American Meteorological*  
551 *Society*, 97(7), pp.1131-1135.  
552  
553  
554  
555  
556  
557  
558  
559  
560  
561  
562  
563  
564  
565  
566  
567  
568  
569  
570  
571  
572  
573  
574  
575  
576  
577  
578  
579  
580  
581  
582  
583  
584  
585  
586  
587  
588  
589  
590  
591  
592



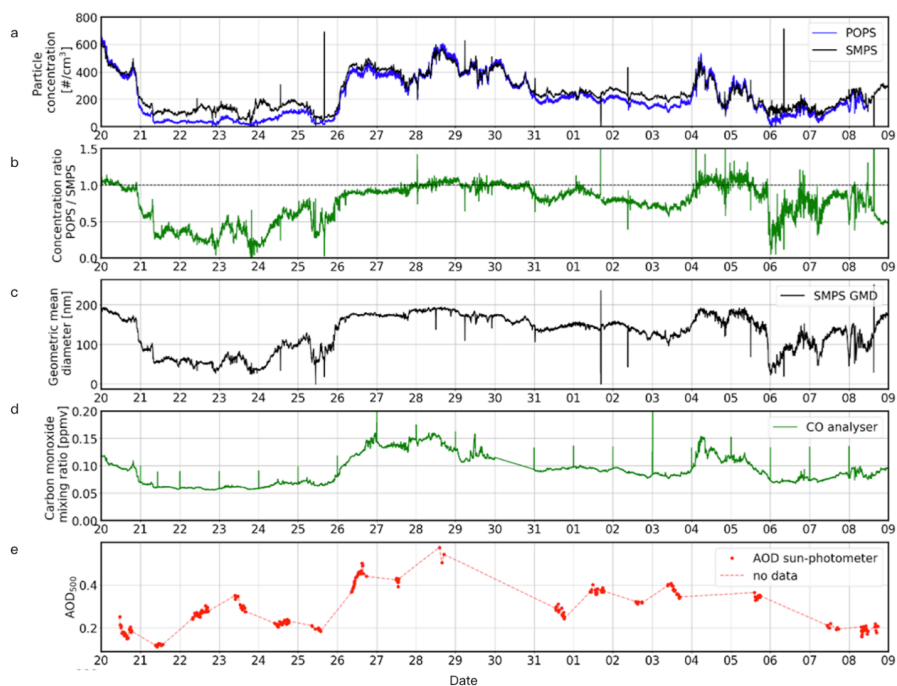
593  
594 **Figure 1.** The DJI Matrice 200 V2 with the POPS (white box at the left bottom of the fuselage).  
595 The red oval shows the inlet tube leading to the POPS.  
596  
597  
598



599  
600 **Figure 2.** PSDs from POPS, SMPS, and data fitted to a wing-mounted PCASP from CLARIFY-  
601 2017 and SAFARI-2000. POPS and SMPS data were collected at the ARM mobile site on Ascension  
602 Island from 20<sup>th</sup> of August to 9<sup>th</sup> of September 2017. The PCASP data from CLARIFY were  
603 collected from a flight on 4<sup>th</sup> of September 2017 (Peers et al., 2019). The PCASP data from SAFARI-  
604 2000 represent a mean from 11 flights performed off the coast of Namibia (Haywood et al., 2003).  
605 Note that the CLARIFY-210 and SAFARAI-2000 PCASP distributions are 'scaled' to the SMPS  
606 size distribution to aid comparison. The POPS and SMPS values are not scaled.



607



608

609 **Figure 3.** From top to bottom. (a) SMPS and POPS total particle concentration. (b) Ratio of POPS  
610 to SMPS total particle concentration. (c) Geometric mean diameter from SMPS. (d) Carbon  
611 monoxide mixing ratio from Los Gatos Research CO analyser, and (e) AOD from Cimel sun-  
612 photometer.

613

614

615

616

617

618

619

620

621

622

623

624

625

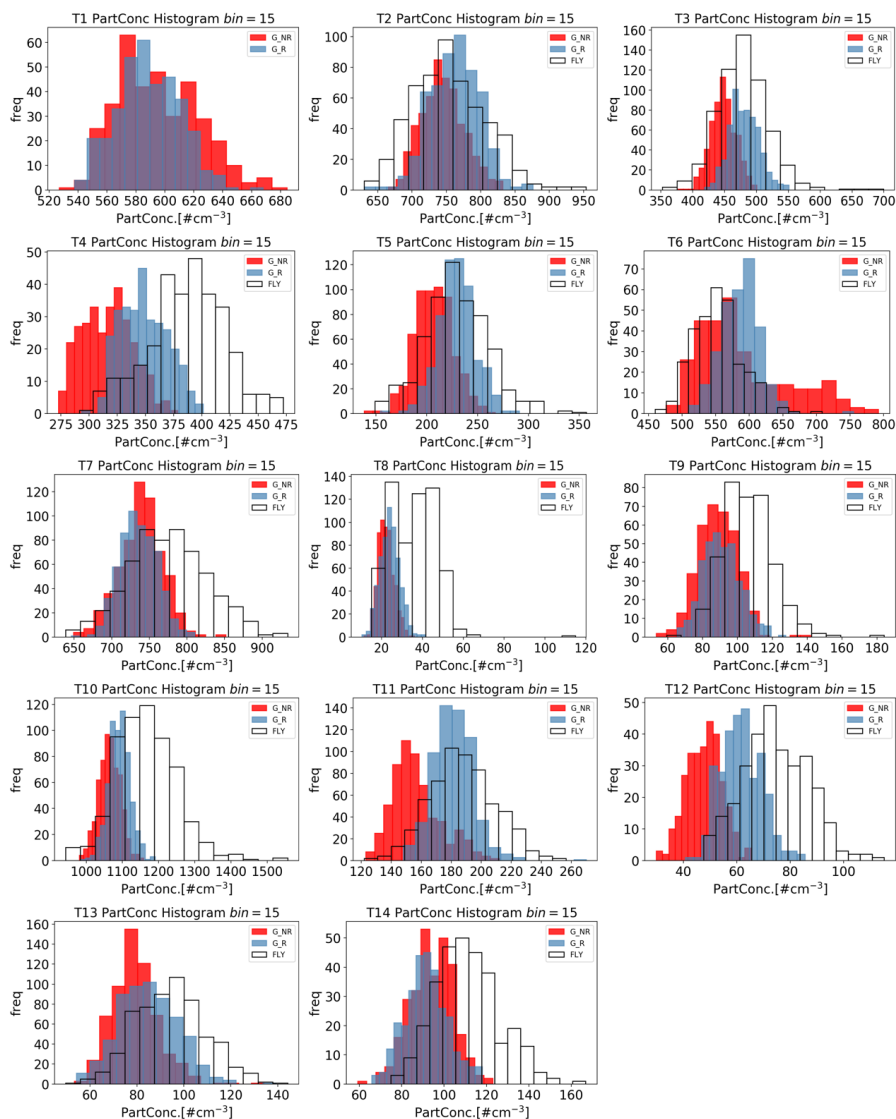
626

627

628

629

630



631

632 **Figure 4.** Probability density functions of PNCs in each case. The bin number was set to 15 for all  
633 stages. Red represents the G\_NR, blue represents G\_R, and white represents FLY.

634

635

636

637

638

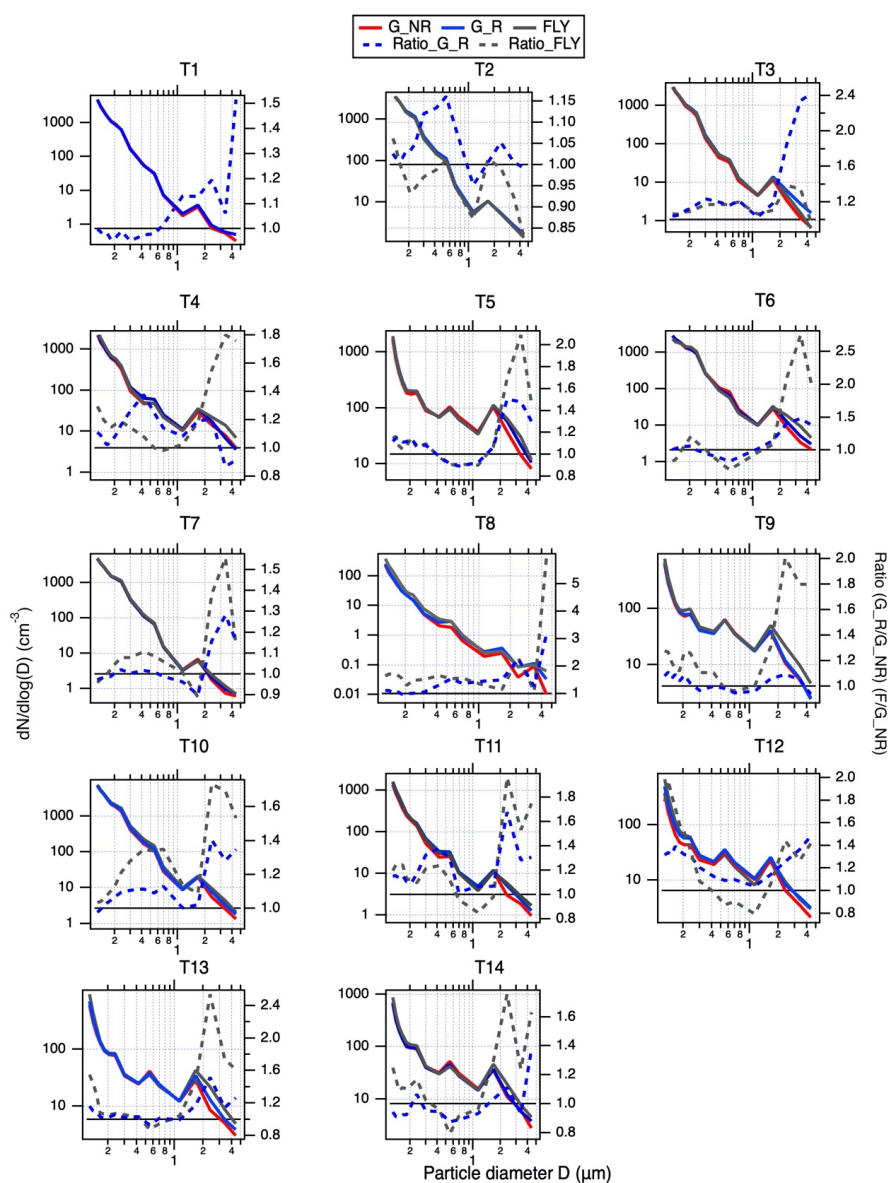
639

640

641



642



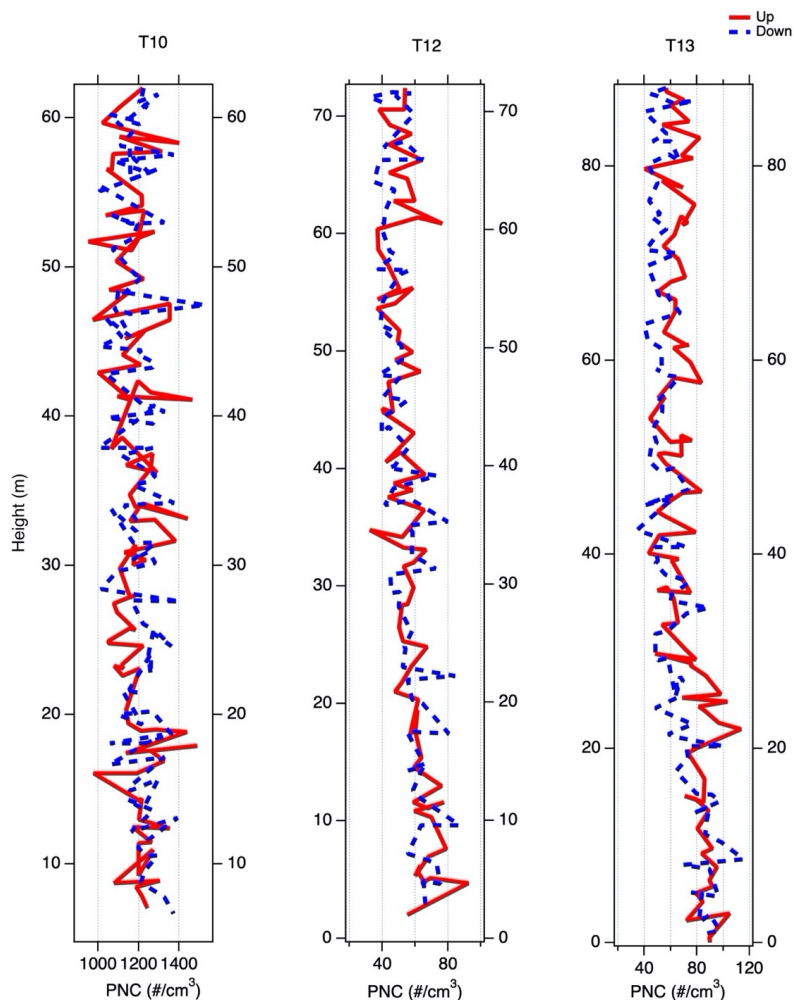
643

644 **Figure 5.** Particle size distribution at three stages: the drone on the ground with rotors off (G<sub>NR</sub>)  
 645 (red line), on the ground with rotors on (G<sub>R</sub>) (blue line) and flying at 10m (FLY) (grey line), in  
 646 each POPS test. The ratios of the PSD at G<sub>R</sub> to G<sub>NR</sub> (blue dash line) and at FLY to G<sub>NR</sub> (grey  
 647 dash line) of each flight are given in each plot.

648

649

650



651  
652 **Figure 6.** Vertical profiles of the particle number concentration in the profile runs of T10, T12,  
653 and T13. The red line shows the observed concentration in the way up and the blue dash line  
654 shows that in the way down, respectively.

655  
656  
657  
658  
659  
660  
661  
662  
663  
664



	Date	Time
T1	18/Nov/2019	16:07 - 16:30
T2	19/Nov/2019	17:00 - 17:35
T3	20/Nov/2019	14:20 - 15:10
T4	25/Nov/2019	10:36 - 11:15
T5	26/Nov/2019	15:21 - 16:00
T6	28/Nov/2019	11:08 - 11:46
T7	2/Dec/2019	11:45 - 12:31
T8	30/Jan/2020	11:49 - 12:34
T9	4/Feb/2020	10:41 - 11:15
T10	7/Feb/2020	11:57 - 12:44
T11	12/Feb/2020	16:35 - 17:26
T12	26/Feb/2020	14:36 - 17:27
T13	3/Mar/2020	11:24 - 12:06
T14	9/March/2020	11:55 - 12:28

**Table 1.** Summary of the dates and time of each test flight.

665  
666  
667  
668  
669  
670  
671  
672  
673  
674

	Initial Height (m)	End Height (m)	Vertical Speed (m/s)
T10	5	60	0.5
T12	5	70	1
T13	2	90	1

**Table 2.** Summary of the initial and end heights and vertical speed of each vertical profile.

675  
676  
677  
678  
679  
680  
681  
682  
683  
684  
685  
686  
687  
688  
689



690

	Date	Particle Number Concentrations (PNCs) ( $\text{cm}^{-3}$ )			Percentage Difference (%)	
		G_NR	G_R	FLY	G_R	FLY
T1	18/Nov/2019	597±30	587±22	n/a	-1.7	n/a
T2	19/Nov/2019	741±52	767±35	742±31	3.5	0.1
T3	20/Nov/2019	442±48	479±23	478±40	8.4	8.1
T4	25/Nov/2019	317±36	349±21	385±30	10.1	21.5
T5	26/Nov/2019	207±19	228±18	230±31	10.1	11.1
T6	28/Nov/2019	567±50	580±30	561±41	2.3	-1.1
T7	2/Dec/2019	753±30	745±24	760±55	-1.1	0.9
T8	30/Jan/2020	22±4	24±5	36±11	9.1	63.6
T9	4/Feb/2020	87±11	91±11	105±19	4.6	20.7
T10	7/Feb/2020	1063±29	1092±29	1169±84	2.7	9.9
T11	12/Feb/2020	156±16	181±13	187±21	16.0	19.9
T12	26/Feb/2020	50±7	63±9	74±11	26	48
T13	3/Mar/2020	79±10	86±13	102±13	8.9	29.1
T14	9/March/2020	95±12	90±10	108±14	-5.3	13.7

691

692

**Table 3.** Summary of the PNCs of each test flight at three stages. n/a = not applicable. The numbers denoted by ±x represent the standard deviation in the PNCs during the measurement time period.

693

694

695

696

697

698

699

700

701

702

703

704

705

706

707

708

709

710

711

712

713

714

715

716



	Surface Wind Speed (m/s)	T test P value	
		G_R	FLY
<b><i>T1</i></b>	0.5	0.2	n/a
<b><i>T2</i></b>	2.6	0.3	0.6
<b>T3</b>	5.7	2e-9	2e-7
<b>T4</b>	3.6	8e-5	2e-7
<b>T5</b>	6.7	2e-9	2e-6
<b><i>T6</i></b>	1.5	0.9	0.2
<b><i>T7</i></b>	1	0.9	0.3
<i>T8</i>	4.1	0.05	3e-6
<i>T9</i>	7.7	0.2	1e-10
<b><i>T10</i></b>	n/a	0.7	0.2
<i>T11</i>	n/a	2e-5	5e-6
<i>T12</i>	n/a	4e-10	1e-6
<i>T13</i>	n/a	0.02	1e-14
<b>T14</b>	n/a	0.2	1e-5

717 **Table 4.** Summary of the dates, time, wind speed, and t test results (p value) of each test flight. Wind  
 718 speed values (at 1.5m) are the wind speed in the hour closest to the experiment time. From T10 to  
 719 T14 the wind speed data is not available (n/a) because the instrument recording the data had broken.  
 720 Flights highlighted in green and bold italic font indicate that the results are not significantly different  
 721 at 5% significance. Flights marked in yellow and italic font indicate that the PNC on the ground  
 722 with the rotor on are not significantly different from G\_NR, and flights marked in red and standard  
 723 font indicate that there are significant differences in both G\_R and FLY when compared to G\_NR.  
 724  
 725  
 726  
 727  
 728

	PNC RMSD (%)	
	G_R	FLY
All cases	10.2	26.2
Low wind speed cases ( $w < 2.6$ m/s)	2.4	5
High wind speed cases ( $2.6 < w < 7.7$ m/s)	12.6	31.4
	PNC MAD (%)	
	G_R	FLY
All flights	7.8	19.1
Low wind speed cases ( $w < 2.6$ m/s)	2.3	3
High wind speed cases ( $2.6 < w < 7.7$ m/s)	10.9	26.3

729 **Table 5.** Summary of RMSD and MAD for all cases, low wind cases, and high wind cases.



	Mean Percentage Difference (%)			
	G_R (%)		FLY (%)	
	Accumulation	Coarse	Accumulation	Coarse
T1	-2.1	17.5	n/a	n/a
T2	5.4	1.6	-0.7	-7.0
T3	10.8	67.4	9.7	17.5
T4	13.3	6.8	15.0	38.3
T5	7.7	19.5	6.4	35.6
T6	-0.8	22.0	-3.6	61.8
T7	-0.3	7.5	3.3	17.2
T8	11.6	83.0	53.2	123.1
T9	4.2	0.9	15.6	48.0
T10	4.9	19.8	14.9	42.4
T11	18.0	23.8	16.8	33.9
T12	25.2	23.0	43.2	14.8
T13	4.2	18.4	13.9	55.5
T14	-5.1	4.5	7.3	29.9
	RMSD (%)			
	G_R		FLY	
	Accumulation	Coarse	Accumulation	Coarse
All cases	10.6	32.2	21.6	49.5
Low wind speed cases ( $w < 2.6$ m/s)	3.4	15.8	7.8	38.6
High wind speed cases ( $2.6 < w < 7.7$ m/s)	12.9	38.5	25.4	53.6
	MAD (%)			
	G_R		FLY	
	Accumulation	Coarse	Accumulation	Coarse
All cases	8.1	22.6	15.7	40.4
Low wind speed cases ( $w < 2.6$ m/s)	2.7	13.7	5.6	32.1
High wind speed cases ( $2.6 < w < 7.7$ m/s)	11.1	27.5	20.1	44.1

730 **Table 6.** Summary of mean percentage differences of size distribution between G\_NR and G\_R,  
 731 and G\_NR and FLY of each flight. The size distributions are separated into two modes:  
 732 accumulation mode ( $0.1 \leq d \leq 1 \mu\text{m}$ ) and coarse mode ( $d > 1 \mu\text{m}$ ).  
 733  
 734  
 735  
 736  
 737  
 738  
 739



	Mean PNCs (cm <sup>-3</sup> )	
	Up	Down
T10	1189±107	1201±101
T12	55±11	54±12
T13	72±15	82±13

740 **Table 7.** Mean PNC with standard deviations on the way up and down in three vertical profile  
741 runs.